On-Site Characterization of Automotive Diffuser Aerodynamics by 3D LPT

Battegazzore, A.; Grille Guerra, A.; Sciacchitano, A.

DOI
10.55037/lxlaser.21st.62

Publication date
2024

Document Version
Final published version

Published in
Proceedings of the 21st International Symposium on the Application of Laser and Imaging Techniques to Fluid Mechanics

On-Site Characterization of Automotive Diffuser Aerodynamics by 3D LPT

Andrea Battegazzore, Adrian Grille Guerra and Andrea Sciacchitano*

Delft University of Technology, Faculty of Aerospace Engineering, Delft, The Netherlands

*a.sciacchitano@tudelft.nl

Keywords: Vehicle Aerodynamics, Field Experiments, Automotive Diffuser, 3D LPT, PIV, Ring of Fire

ABSTRACT

This investigation proposes a novel LPT facility featuring Helium-Filled Soap Bubbles flow tracers, LED illumination and two high-speed cameras to characterize the dominating flow patterns within automotive underbodies. A remote control (RC) car model, fitted with custom-made floor and diffusers, traverses a region of seeded air following the Ring of Fire methodology. Underground-placed cameras view the car through a transparent panel, providing unparalleled optical access to the underbody of the car. The on-site measurement setup and the interaction between car model and ground enhance the realism and fidelity of the experiment, while potentially reducing testing costs associated with wind tunnel operation. The setup is shown to be a valid alternative to conventional testing grounds to capture flow separation, 3D flow topology and differences in the flow field between the four tested configurations, whereby the diffuser angle was varied in the range between 5° and 20°. The 15° diffuser led to the highest peak velocity ($u/U = 1.3$) in the underbody, whereas the 10° diffuser produced the largest downforce; the 20° diffuser showcased the most prominent flow separation at the diffuser leading edge, heavily affecting the diffuser's ability to accelerate the flow in the car's underbody. The results highlight the impact of the tyres in counteracting the ground effect and thus the formation of low-pressure regions under the vehicle, leading to mass flow leakage through the sides of the car and a significant disruption to the mechanism of downforce generation.

1. Introduction

Race cars use aerodynamic downforce to increase the friction between the tyres and the road, thus enhancing the cornering speed and in turn reducing the lap times. The underbody typically contributes to about 50% of the total downforce generated by race cars, with the remaining 50% achieved by the front and rear wing assemblies (Toet, 2013). Diffusers are often employed in the underbodies of race cars to increase the downforce. A diffuser is a diverging duct that converts the flow's kinetic energy into a pressure rise. In automobiles, the diffuser usually consists of an upswept ramp located at the aft of a vehicle's underbody. Early studies on the aerodynamics of diffusers were conducted by Cooper et al. (1998), who identified three physical mechanisms by which diffusers contribute to a car's downforce, namely pumping, upsweep and ground interaction. Because the flow at the outlet of a diffuser has a fixed base pressure close to the atmospheric pressure, the diffuser makes use of the Venturi effect to decrease the flow's static pressure at the car's underbody, thus acting as a "pump down" mechanism (Ehirim et al., 2019). Additionally, the upswept shape of the diffuser adds a negative camber effect to the vehicle's body, with the underbody acting as the suction

side of a wing. Finally, the car's underbody operates in close proximity to the ground: because of continuity, the ground constraint causes the underbody flow to accelerate, thus resulting in lower static pressure based on the Bernoulli's principle and therefore the production of a downforce. It is important to note that longitudinal vortices are formed at the lengthwise edges of the diffuser because of the pressure difference between the outer flow and the underbody flow; the strength and breakdown of those vortices influence the static pressure distribution along the diffuser and in turn the downforce generated (George and Denis, 1983).

The aerodynamic performances of diffusers in ground effect have been investigated experimentally by force balance measurements (George, 1981; Ruhrmann and Zhang, 2003) as well as by surface pressure measurements (Senior, 2002; Ruhrmann and Zhang, 2003). Oil flow visualization and Laser Doppler Velocimetry (LDV) measurements have been proven useful to understand the diffuser flow topology (Senior, 2002; Cooper et al., 1998). Considering the many obstructions (ground, wheels and the car itself) that hinder optical access to the underbody of the vehicle and the necessary simplifications often employed (no wheels, small scale), little research has been done in this region using PIV or PTV methods. PIV has been employed by Senior (2002) and Jowsey (2013) to characterize the strength and location of the longitudinal vortices. However, the use of more recent and advanced particle tracking approaches for the study of automotive diffuser flows is not reported in the literature.

Thanks to the recent introduction of sub-millimetre helium-filled soap bubbles (HFSB) flow tracers (Scarano et al., 2015), PIV measurements have been conducted in planes as large as several squared metres, notably for the on-site characterization of the wakes of cyclists (Spoelstra et al., 2019), ice-skaters (Spoelstra et al., 2023) and automobiles (Hütting et al., 2023) via the so-called *Ring of Fire* approach. The recent advancements in three-dimensional Lagrangian Particle Tracking (LPT) via the robust and time-efficient Shake-The-Box algorithm (STB, Schanz et al., 2016) open new possibilities for the quantitative visualization of three-dimensional flow fields.

The objective of this investigation is to construct and demonstrate a 3D LPT experimental setup that leverages Ring of Fire methodologies to characterize the three-dimensional flow inside automotive diffusers. Since a wide range of flow characteristics can be replicated with relatively simple geometry changes, a range of diffuser angles (θ) that are expected to show a variety of flow patterns are selected and tested. More specifically, the study aims at determining the diffuser angle that produces the largest downforce, thus identifying the relationship between diffuser angle and flow topology in the car's underbody.

2. Diffuser aerodynamics

2.1. Related works

The aerodynamic performances of the automotive diffusers are strongly affected by the diffusers' geometrical characteristics (Ehirim et al., 2019), namely the area ratio (ratio between diffuser's outlet and inlet areas), the length, the ride height and the diffuser angle. By performing surface pressure

and force measurements, Cooper et al. (1998, 2000) indicated that the optimum geometry of diffusers depends on the ground boundary condition, and in particular on whether the ground is fixed or moving; the authors concluded that, for a given diffuser length, a given pressure recovery can be achieved with smaller diffuser area ratio using a moving ground rather than a fixed ground. While, theoretically, reducing the ride height always enhances the underbody suction and thus increases the downforce, in practice four distinct flow regions were identified by Senior (2002): (i) the *downforce enhancement* region, occurring for $h/d \geq 0.32$, being h the underbody's height relative to the ground and d the underbody's half width; (ii) the *maximum downforce* region, for $0.2 \leq h/d < 0.32$; (iii) the *downforce reduction* region around $0.15 < h/d < 0.2$: the reduction of downforce is generally attributed to the breakdown of the longitudinal vortices as well as to the interaction between the ground and underbody boundary layers, which thus reduce the mass flow in the underbody area; (iv) the *downforce loss* region, occurring for h/d smaller than 0.15.

The diffuser angle affects the strength and break-down of the longitudinal vortices as well as the presence of flow separation in the diffuser. In their wind tunnel study, Ruhrmann and Zhang (2003) found that the flow remains attached for diffuser angles below 5 degrees, while at higher angles a separation bubble is formed. Furthermore, the maximum downforce was achieved at an angle of 20 degrees. Conversely, Jowsey and Passmore (2010) reported a maximum downforce at a diffuser angle of 13 degrees, while the higher diffuser angles yielded lower downforce. The contrasting results between the two studies above are attributed to the differences in ground boundary conditions (Ehrim et al., 2019): in fact, Ruhrmann and Zhang (2003) performed measurements with a moving ground, whereas Jowsey and Passmore (2010) made use of a fixed ground.

2.2. Conceptual model

A simplified conceptual model based on mass conservation is introduced to link the current state of literature on diffuser aerodynamics with the flow patterns expected from this study. An area-based 1D duct representation of the underbody of a vehicle is simulated. For this simplified analysis, the flow is assumed to be inviscid, incompressible and irrotational. Due to continuity, the mass flow through this duct is constant: $\dot{m} = \rho A u$ and $\dot{m}/\rho = Au = constant$. Using Bernoulli's equation, the following definition of C_p can be obtained (Anderson, 2017), being U the free-stream velocity in the car's frame of reference:

$$C_p = 1 - \left(\frac{u}{U}\right)^2$$

As mass flow and density are constant, the pressure coefficient at any spanwise location of the duct is dependent only on the area ratio at the chosen location: $\frac{u(x)}{U} = \frac{A_\infty}{A(x)}$, whereby $A_\infty$is the area (which in the 1D case corresponds to the channel height) where free-stream conditions are met. In the example here, the channel height is chosen equal to $h = 20\ mm$, and $A_\infty = \frac{5}{2}h = 50\ mm$. The variation of the pressure coefficient along the car's underbody can be expressed as $C_p(x) = 1 - \left(\frac{A_\infty}{A(x)}\right)^2$. Clearly, if $A = A_\infty$, then the pressure coefficient is null; as A decreases, C_p becomes negative due to the

streamwise acceleration. The pressure at the diffuser outlet is fixed at p_∞ (or $C_p = 0$) to simulate perfect expansion and recovery to free-stream conditions. Ignoring flow separation, the flow speed can be evaluated backwards from the diffuser outlet up to the channel's entrance. Because of the assumptions made (inviscid, incompressible and irrotational flow), the diffuser's area ratio dictates the pressure and speed throughout the whole domain.

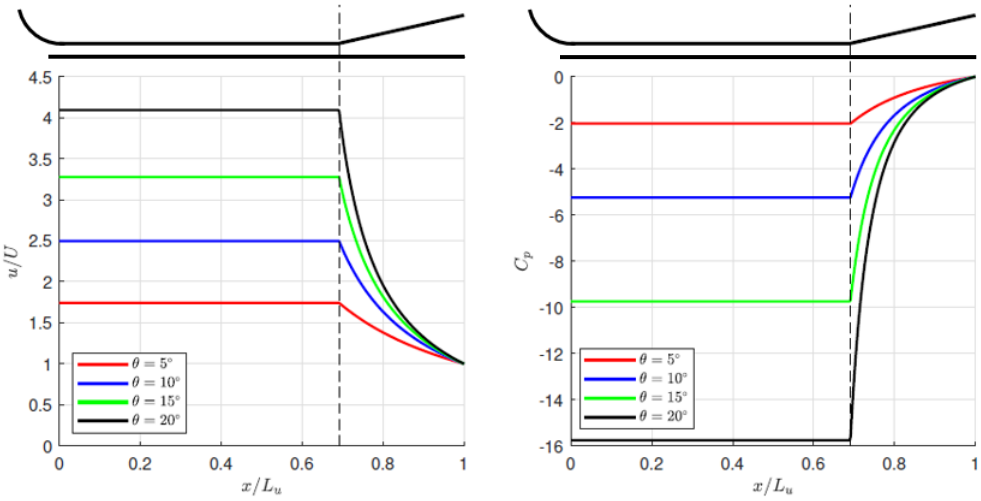

Figure 1. Streamwise evolution of the normalized flow velocity (left) and pressure coefficient (right) for different diffuser angles, assuming fixed pressure ($C_p = 0$) at the diffuser outlet.

Figure 1 shows the effect of changing the diffuser angle on the pressure and velocity in the floor and diffuser portion of the duct. Here the spatial coordinate is normalized with the underbody length (L_u). As expected, increasing the diffuser angle allows for a lower pressure to be maintained through the floor region.

3. Methodology

3.1. Experimental setup and testing routine

The experiments were performed in the Flow Physics and Technology Laboratories of Delft University of Technology in the Netherlands. The vehicle used in the experimental campaign is a radio-controlled battery-powered scaled vehicle. This wheeled car is 505 mm long, 365 mm wide, 175 mm tall and weighs 2.5 kg. This vehicle was fitted with a custom-made 200 mm wide and 370 mm long flat floor. Four 3D printed diffusers with side plates, 180 mm long and with varying angles (5°, 10°, 15° and 20°), were designed to be mounted and swapped. Figure 2 shows the vehicle painted and fitted with the 5° diffuser. The total length of the underbody, including flat floor and diffuser, was $L_u = 550$ mm. The nominal height of the underbody relative to the ground was $h = 20\,mm$, resulting in $h/d = 0.2$, being $d = 100\,mm$ the underbody half-width. A view of the flat floor with three rows of white markers is shown in Figure 2-left. These markers were used in the processing phase to track the speed and position of the car in order to align different tracks with each other. The test speed was limited on the remote controller to better control the position of the vehicle and minimize bouncing. The average test speed was measured to be 6 m/s, resulting in a Reynolds number $Re = 220{,}000$ based on the underbody length.

Figure 2. Pictures of the RC car. Left: underbody with markers and annotated dimensions in cm. Right: RC car with 5° diffuser.

The experimental setup was designed to provide visual access to the car's underbody; a schematic is shown in Figure 3.

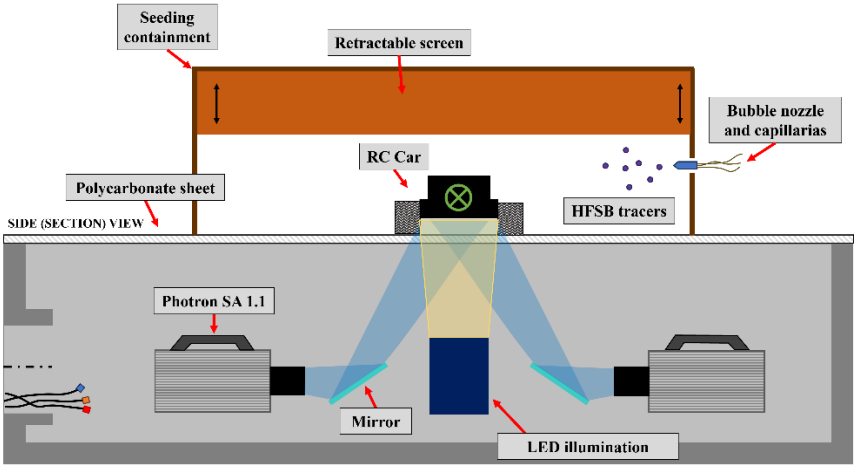

Figure 3. Schematic of the experimental setup.

A concrete shell with an internal volume of 2 m (length) by 43 cm (width) by 40 cm (height) was placed in the ground, with its longest dimension perpendicular to the direction of motion of the RC car. Inside the shell, two Photron SA1.1 cameras (12 bit, 20 µm pixel pitch, 1,024×1,024 pixels) and one LaVision LED light source were mounted. Each camera faced a mirror that allowed it to view the same portion of the vehicle's diffuser through a transparent 12 mm thick polycarbonate sheet. The cameras mounted 35 mm lenses set at an $f_{\#}$ of 16, achieving a square field of view of 20 cm × 20 cm at the location of the transparent sheet. To limit unwanted light reflections, the LED light source was equipped with a slit. The area (perpendicular to light propagation direction) where particles were

illuminated was 8 cm (lateral direction) × 20 cm (streamwise direction). With this setup, the field of view was insufficient to observe the full width of the diffuser and floor; multiple passages of the car were conducted to measure the flow in the entire underbody. The flow was seeded with Helium-filled soap bubbles (HFSB) flow tracers released by a single home-made generator. To achieve sufficient concentration of flow tracers, the HFSBs were confined in a wooden construction 50 cm tall, 120 cm wide and 70 cm long. The entrance and exits of this wooden construction could be opened and closed with two roll-up curtains to accumulate the bubbles and then allow the passage of the car. Running the bubble generator for 1 minute was required to achieve the target bubble density of 1 bubble/cm^3.

After camera calibration, the data acquisition could start by operating the HFSB generator with the curtains down. As the car begun its motion, one operator lifted the curtains up fully. At a distance of 40 cm before the entrance of the measurement domain, the vehicle tripped a laser photodetector, which in turn triggered the image acquisition by the cameras. For each passage, 300 image pairs were captured at 1000 Hz. A view from inside the seeding containment box before the passage of the car and with the car in view is shown in Figure 4. Repeating this procedure 20 times per diffuser angle allowed for the generation of a sufficiently large set of images to achieve statistical convergence. The time between two successive passages of the car was about 3 minutes.

Figure 4. Illustration of the measurement domain before (left), during (middle) and after (right) the passage of the car.

3.2. Data processing

To remove unwanted light reflection and enhance the particles detectability, a frequency high-pass Butterworth filter (Sciacchitano and Scarano, 2014) was employed. Then, the images were processed via the Shake-The-Box LPT algorithm (Schanz et al., 2016) to obtain three-dimensional particle tracks. Image recording and processing was conducted with the DaVis 10 software from LaVision GmbH.

3.2.1. Galilean Transformation

A Galilean transformation was used to convert the tracks position and velocity information from the lab (static) frame of reference to the car (moving) frame of reference. The coordinates in the lab frame of reference are indicated with (X', Y', Z'), and the corresponding flow velocities are (u', v', w'). The vehicle's frame of reference, whose coordinates and flow velocities are indicated with (X, Y, Z) and (u, v, w), respectively, moves with the vehicle at a speed equal to it, denoted as U. The speed of the car was evaluated via the markers placed in the car's underbody. A key snapshot t^*, where the last marker on the car's floor is in view, is introduced. The location of the markers at this key frame, in the laboratory frame of reference, is denoted as $X^*_m = {X'}_m(t^*)$ and $Y^*_m = {Y'}_m(t^*)$. The XY location of the last marker of the central row is also the location of the origin of the vehicle's coordinate system, and

corresponds to the leading edge of the diffuser in the car's symmetry plane: $O_X = X_m^*$ and $O_Y = Y_m^*$. The vertical location of the origin of the vehicle's coordinate system is set on the ground. Hence, the equations of the Galilean transformation are:

$$\begin{cases} X(t) = X'(t) - X_m^* + U \cdot (t - t^*) \\ Y(t) = Y'(t) - Y_m^* \\ Z(t) = -Z'(t) \end{cases} \quad \begin{cases} u(t) = U + u'(t) \\ v(t) = v'(t) \\ w(t) = -w'(t) \end{cases} \tag{1}$$

Note that the direction Z is flipped with respect to the laboratory's frame to align positive Z upwards. An example of application of the Galilean transformation is reported in Figure 5.

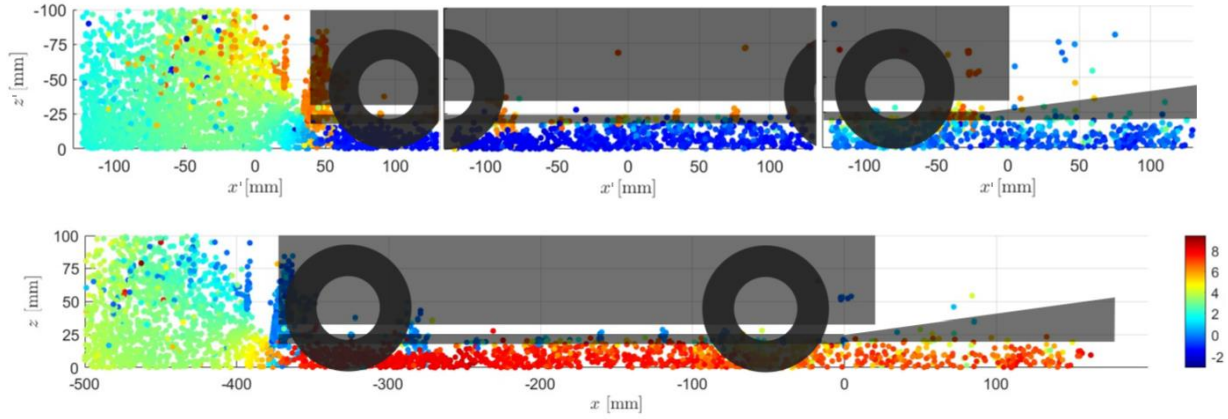

Figure 5. Example of the application of the Galilean transformation. Top: before the transformation, considering three time instants with the car entering the measurement domain (left), in the middle of the measurement domain (middle) and exiting the measurement domain (right). Bottom: after the transformation. The colorbar indicates the streamwise velocity in meters per second.

3.2.2. Data averaging

The velocity information from multiple car's passages is combined together in the car's frame of reference, after having normalized the velocity of each run by the car's speed to correct for small velocity variations among different runs. The velocity data is then averaged in time and mapped onto a Cartesian grid using the spatial averaging procedure discussed in Agüera et al. (2016). The selected bin size was 15 mm with 75% overlap between adjacent bins, resulting in a vector spacing of 3.75 mm.

4. Results

A three-dimensional view of the flow field for the θ = 15° diffuser case is illustrated in Figure 6**;** from this figure, it is already possible to see the stagnation of the flow in the front of the car, the acceleration in the underbody region, where the air speed exceeds the car speed, and the three-dimensional flow in the car wake.

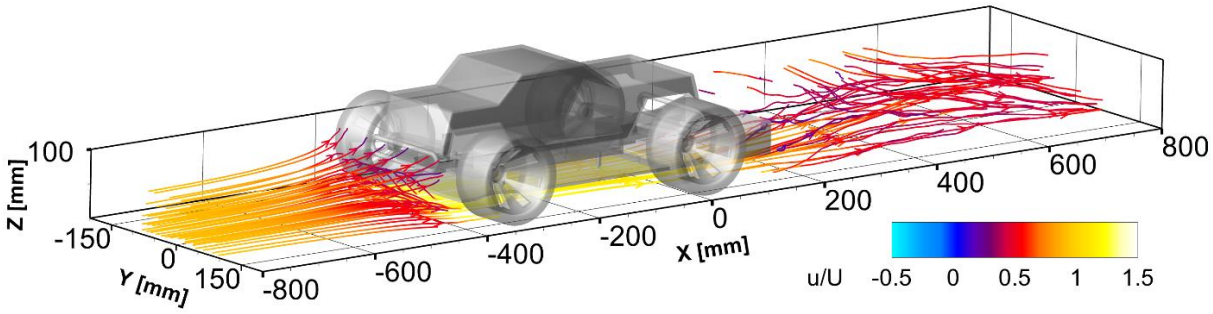

Figure 6. Three-dimensional view of the car model with $\theta = 15°$ diffuser, showing the 3D streamlines colour-coded by streamwise velocity (normalized with respect to the car velocity).

4.1. Streamwise velocity

To highlight the differences among the different diffuser configurations, the contours of the streamwise velocity u/U in the car's symmetry plane ($Y = 0$) are shown in Figure 7. For all diffuser angles, the flow under the car is characterized by a general streamwise acceleration starting at the inlet of the underbody. To varying extents, all cases present high-velocity peaks at $X \approx -350$ mm and $X \approx 0$ mm. These local maximums of u/U are situated at the floor's inlet region and at the diffuser inlet, respectively; their locations are referred to as first and second peak locations, respectively. The flow speed under the car increases with the diffuser angle until $\theta = 15°$, which presents the strongest velocity peaks of $u/U = 1.32$ for both the first and second maximums. Despite the $\theta = 20°$ diffuser entailing the largest outlet area, this geometry is not able to produce additional suction under the car, likely due to strong separation of the flow. A boundary layer, marked by the growth of a low-speed region from around $X = -250$ mm, can be observed on the car's floor for all diffuser geometries.

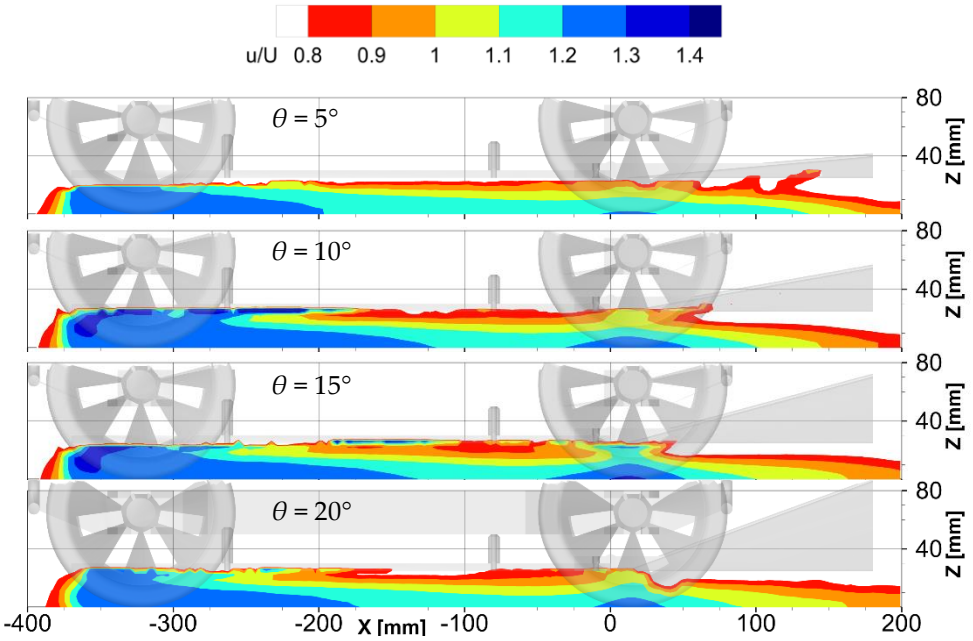

Figure 7. Contours of the streamwise velocity component at the car's symmetry plate ($Y = 0$) for the four diffuser angles (from top to bottom: $\theta = 5°$, 10°, 15° and 20°).

4.2. Spanwise velocity

Figure 8 illustrates the spanwise velocity component (v/U) on a Z-slice 10 mm from the ground for the diffuser with $\theta = 15°$. In the region before the car ($X < -400\,mm$), the streamlines deflect consistently outwards because of the adverse pressure gradient induced by the stagnation in front of the car. At around $X = -250$ mm, after the stagnation region, two bubbles of inflow are visible, symmetric with respect to the car's median plane.

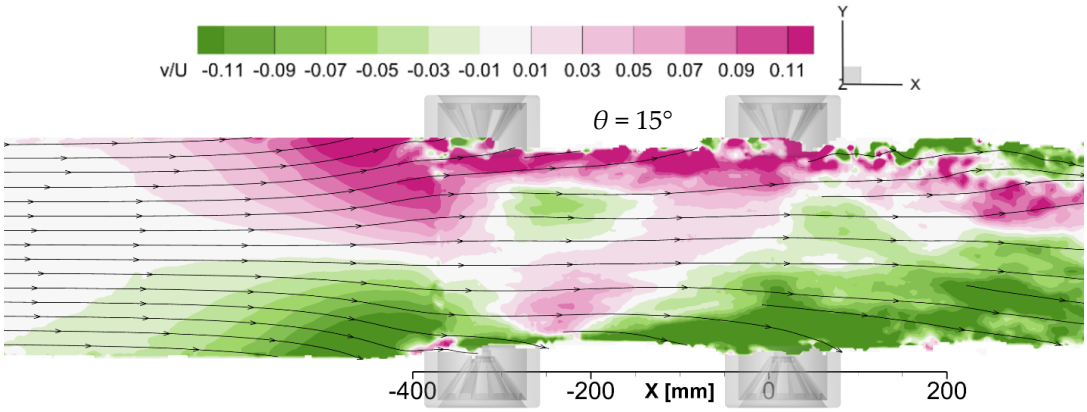

Figure 8. Contour of spanwise velocity component and velocity streamlines at Z = 10 mm for the diffuser angle θ = 15°.

These inflow bubbles are associated with the low pressure occurring in the car's underbody because of the local flow acceleration. The presence of this low-pressure region is highlighted by the local straightening and contraction of the streamlines at $-400\,mm < X < -200$ mm. From around $X = -200$ mm, a gradually expanding region of outward-moving flow, originating from the sides of the floor and growing towards the centre, dominates the domain. This outward motion is caused by the presence of the tyres: these large flow-obstructing appendices generate a large wake of turbulent and low-pressure region that causes air spillage from beneath the car's floor.

4.3. Flow in the diffuser region

One key indicator to detect flow separation and differentiate the performance of the diffuser geometries is the flow direction in the diffuser region. This is depicted in Figure 9, where the streamlines are superimposed onto the contours of the streamwise velocity component u/U in the diffuser region. As expected, the flow in the diffuser moves upwards, following the expansion caused by the change in cross-sectional area. In the case of $\theta = 5°$ and $\theta = 10°$, the flow expands following the geometry of the diffuser, thus indicating that the flow remains attached to the underbody's surface. At the higher angles ($\theta = 15°$ and $\theta = 20°$), the streamlines also expand, but exhibit a clear curvature which is ascribed to the flow separation at the diffuser leading edge. Because of the limited extent of the seeded region in the experimental setup, the recirculation bubble that forms close to the diffuser's surface is void of tracer particles; hence, flow velocity measurements are not possible there.

Downstream of the diffuser, a wake region is formed, enclosed between the shear layers stemming from the car's underbody and top surface. The extent of the wake region decreases with increasing diffuser angle as a result of the larger upward deflection of the flow exiting the diffuser. For the lower

diffuser angle of $\theta = 5°$, the car wake region does not contain any flow tracers, thus precluding any velocity measurements in it.

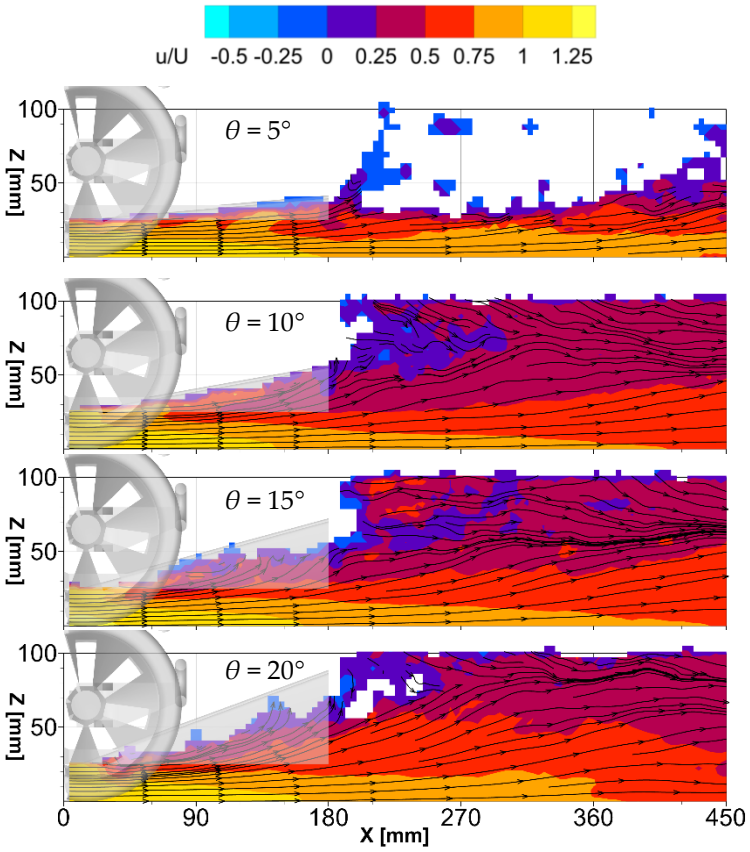

Figure 9. Contours of the streamwise velocity component with streamlines in the diffuser region at the car's symmetry plate ($Y = 0$) for the four diffuser angles (from top to bottom: θ = 5°, 10°, 15° and 20°).

4.4. Pressure distribution and downforce

Following the methodology developed and explained in section 2.2, the C_p distribution is evaluated in the midplane, on a straight line parallel to the ground and at a distance of 12.5 mm (or 0.023 L_u) from it. The results are shown in Figure 10. Here, the planar velocity component and C_p are plotted along the normalized streamwise coordinate (X/L_u). Annotations above the plots mark the ground (straight continuous horizontal line), the underbody surface and the probe line (dash-dotted line) on which data is extracted. The data shows how the floor region prior to the diffuser ($0 \leq X/L_u \leq 0.7$) is responsible for almost all the low pressure in the underbody, while in the diffuser region ($0.7 < X/L_u \leq 1$) a pressure recovery occurs, whereby the pressure increases to values above free-stream conditions.

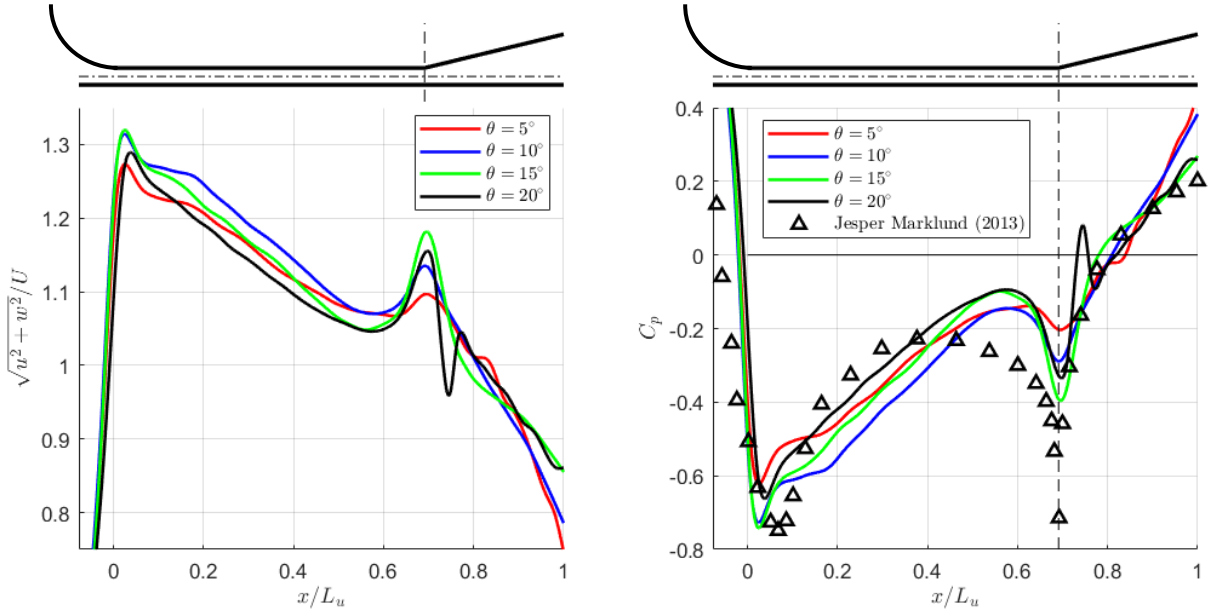

Figure 10. Planar velocity magnitude (left) and C_p (right) distributions on a straight line parallel to the ground and at a distance of 12.5 mm (or 0.023 L_u) from it.

All diffuser geometries feature two high-velocity (low-pressure) peaks at the leading edges of the underbody and of the diffuser, respectively, and a rapid expansion in the diffuser. The diffuser pumping effect mentioned earlier leads to different velocities and pressure distributions under the floor depending on the diffuser angle. The relative heights of the peaks between diffusers matches those already discussed in section 4.1. All velocity curves present a steady decrease right after the first peak: this can be explained by the effect of the front tyres, which induce low-pressure regions in their wakes that causes a deflection of the flow from the median plane of the underbody outwards, thus resulting in a flow deceleration in the median plane. As a consequence, the static pressure increases in this region. The second velocity peak occurs at the leading edge of the diffuser ($X/L_u = 0.67$): such peak is associated with a low-pressure peak responsible for the curvature of the streamlines, thus allowing the flow to deflect upwards, following the geometry of the diffuser. In the diffuser, the flow expands, yielding a reduction in the flow velocity and an increase in static pressure. For all diffuser configurations, the flow at the diffuser outlet reaches a pressure higher than p_∞ (or $C_p > 0$), which is attributed to the turbulent wake formed downstream of the car.

The pressure results of Figure 10-right also present a comparison with surface pressure measurements conducted in a wind tunnel by Marklund (2013) on an Ahmed body with a 9.4° diffuser angle ($Re = 1.7 \cdot 10^6$ based on the model's length). The comparison between current results and literature data exhibits good agreement, although the LPT-based pressure peaks are broader and lower, especially at the diffuser's inlet, because of the finite size of the interrogation bin (15 mm) used for averaging the velocity information.

Finally, the static pressure is integrated all over the car's underbody, including the diffuser, to evaluate its contribution to the generated downforce. Notice that, because the static pressure in the underbody region is mainly lower than p_∞, the generated vertical force is directed downwards. For

this reason, the magnitude of the downforce F_Z is reported in Table 1. The results show that the maximum downforce is produced at the diffuser angle of 10°, which is consistent with the higher flow velocity and lower static pressure at the median plane, as discussed previously in this section. Instead, the highest diffuser angle $\theta = 20°$ yields the minimum downforce, whose magnitude is similar to that obtained at the lowest diffuser angle $\theta = 5°$. This result is ascribed to the flow separation occurring at the diffuser's leading edge for $\theta = 20°$, which reduces the mass flow in the underbody region and therefore the flow acceleration and the generated suction.

Table 1. Downforce generated by the car's underbody in the different diffuser configurations.

Diffuser angle θ	**5°**	**10°**	**15°**	**20°**
$\lvert Fz\ (N)\rvert$	0.35	0.57	0.48	0.32

5. Conclusions

A novel Lagrangian Particle Tracking (LPT) facility was designed and constructed for the study of the aerodynamics of automotive diffusers. The facility featured Helium-Filled Soap Bubbles flow tracers and underground imaging and illumination through a transparent ground pate. Measurements were conducted using the Ring of Fire approach (Spoelstra et al., 2019), whereby an RC car, fitted with custom-made floor and diffusers of angles between 5° and 20°, traversed a region of seeded air. Particle tracks from multiple runs (≥ 20 for each diffuser), obtained with the Shake-the-Box (Schanz et al., 2016) LPT algorithm, were first mapped onto the vehicle's moving frame of reference with a Galilean transformation, and then averaged in time and space within bins of 15 mm size.

The setup was shown to be a valid alternative to conventional testing approaches to capture flow separation, 3D flow evolution and differences in the flow field between the diffusers with varying angles. The 15° diffuser led to the largest velocity and pressure peaks under the car, whereas the 10° diffuser produced the most downforce thanks to the diffuser "pumping" effect, leading to a large region of low pressure under the vehicle. Notably, the 20° diffuser featured the most prominent flow separation at the diffuser's leading edge, heavily affecting its ability to sustain low pressures under the car. The results showed that the wide tyres have a major impact on the underbody flow, because their large wakes induce mass flow leakage through the sides of the car, thus disrupting the mechanism of downforce generation and impairing the generation of streamwise vortices.

References

Agüera, N., Cafiero, G., Astarita, T., & Discetti, S. (2016). Ensemble 3D PTV for high resolution turbulent statistics. Measurement Science and Technology, 27(12), 124011.

Anderson, J. D. (2017). Fundamentals of Aerodynamics. McGraw-Hill Education.

Cooper, K. R., Bertenyi, T., Dutil, G., Syms, J., & Sovran, G. (1998). The aerodynamic performance of automotive underbody diffusers. SAE transactions, 150-179.

Cooper, K. R., Syms, J., & Sovran, G. (2000). Selecting automotive diffusers to maximise underbody downforce. SAE transactions, 497-512.

Ehirim, O. H., Knowles, K., & Saddington, A. J. (2019). A review of ground-effect diffuser aerodynamics. Journal of Fluids Engineering, 141(2), 020801.

George, A. R. (1981). Aerodynamic effects of shape, camber, pitch, and ground proximity on idealized ground-vehicle bodies. J. Fluids Eng.103(4): 631-637.

George, A. R., & Donis, J. E. (1983). Flow patterns, pressures, and forces on the underside of idealized ground effect vehicles. In Proceedings of the ASME Fluids Engineering Division Symposium on Aerodynamics of Transportation-II (Vol. 7, pp. 69-79).

Hüttig, S., Gericke, T., Sciacchitano, A., & Akkermans, R. A. D. (2023). Automotive on-road flow quantification with a large-scale Stereo-PIV setup. Presented at the *15th International Symposium on Particle Image Velocimetry*, San Diego, California, 19-21 June 2023.

Jowsey, L., & Passmore, M. (2010). Experimental study of multiple-channel automotive underbody diffusers. Proceedings of the Institution of Mechanical Engineers, Part D: Journal of Automobile Engineering, 224(7), 865-879.

Jowsey, L. (2013). An experimental study of automotive underbody diffusers (Doctoral dissertation, Loughborough University).

Marklund, J. (2013). Under-body and diffuser flows of passenger vehicles. Chalmers Tekniska Hogskola (Sweden).

Ruhrmann, A., & Zhang, X. (2003). Influence of diffuser angle on a bluff body in ground effect. J. Fluids Eng., 125(2), 332-338.

Scarano, F., Ghaemi, S., Caridi, G. C. A., Bosbach, J., Dierksheide, U., & Sciacchitano, A. (2015). On the use of helium-filled soap bubbles for large-scale tomographic PIV in wind tunnel experiments. Experiments in Fluids, 56, 1-12.

Schanz, D., Gesemann, S., & Schröder, A. (2016). Shake-The-Box: Lagrangian particle tracking at high particle image densities. Experiments in fluids, 57, 1-27.

Sciacchitano, A., & Scarano, F. (2014). Elimination of PIV light reflections via a temporal high pass filter. Measurement Science and Technology, 25(8), 084009.

Senior, A. E. (2002). The aerodynamics of a diffuser equipped bluff body in ground effect (Doctoral dissertation, University of Southampton).

Spoelstra, A., de Martino Norante, L., Terra, W., Sciacchitano, A., & Scarano, F. (2019). On-site cycling drag analysis with the Ring of Fire. Experiments in Fluids, 60, 1-16.

Spoelstra, A., Terra, W., & Sciacchitano, A. (2023). On-site aerodynamics investigation of speed skating. Journal of Wind Engineering and Industrial Aerodynamics, 239, 105457.

Toet, W. (2013). Aerodynamics and aerodynamic research in Formula 1. The Aeronautical Journal, 117(1187), 1-26.

Wieneke, B. (2008). Volume self-calibration for 3D particle image velocimetry. Experiments in fluids, 45(4), 549-556.

Zhang, X., Toet, W., & Zerihan, J. (2006). Ground effect aerodynamics of race cars. Applied Mechanics Reviews 59: 33-49.